

Stacking dependent ferroelectricity and antiferroelectricity in quasi-one-dimensional oxyhalides NbOX_3

Wencong Sun¹, Ning Ding¹, Jun Chen¹, Hai-Peng You², Jin Peng¹, Shan-Shan Wang^{1,*} and Shuai Dong^{1†}

¹*School of Physics, Southeast University, Nanjing 211189, China and*

²*School of Science, Changzhou Institute of Technology, Changzhou 213032, China*

(Dated: October 11, 2022)

Low-dimensional ferroelectricity and polar materials have attracted considerable attentions for their fascinating physics and potential applications. Based on first-principles calculations, here we investigate the stacking modes and polar properties of a typical series of quasi-one-dimensional ferroelectrics: double-chain oxyhalides NbOX_3 ($X=\text{Cl}, \text{Br}, \text{and I}$). The geometry of their double-chains allows both the interchain/intrachain permutation. Thus, different stacking modes of double-chains lead to a variety of ferroelectric and antiferroelectric phases in both the tetragonal and the monoclinic crystals. The proximate energies of these phases may lead to multiphase coexistence in real materials, as well as the hydrostatic pressure driving structural phase transition. Their spontaneous polarizations and piezoelectricity of the ferroelectric phases are prominent, comparable to commercially used ferroelectric BaTiO_3 and piezoelectric ZnO , respectively. Our paper demonstrates that the van der Waals NbOX_3 are promising materials for exploring quasi-one-dimensional ferroelectricity and antiferroelectricity.

I. INTRODUCTION

Ferroelectrics with spontaneous electric polarizations have stimulated great interests in condensed matter and material communities, due to their significant scientific importance and wide applications in devices [1–3]. Especially, the piezoelectric properties of ferroelectrics enable the interconversion between force/pressure and electrical signals, leading to various electromechanical sensors and actuators [4–6]. Especially, the intrinsic piezoelectric coefficients of ferroelectric (FE) materials are significantly enhanced near the morphotropic phase boundary (MPB) between two proximate phases with similar crystallographic structures but different polarities [7]. Most studies on MPB's have been performed on ferroelectric perovskites, such as $\text{Pb}(\text{Zr}_x\text{Ti}_{1-x})\text{O}_3$ and $(\text{PbMg}_{1/3}\text{Nb}_{2/3}\text{O}_3)_{1-x}(\text{PbTiO}_3)_x$ [8, 9]. Recently, MPB's have also been identified or predicted in simpler compounds, such as BaTiO_3 , PbTiO_3 [10, 11], as well as a GeS monolayer [12].

When FE-related devices are reduced to nanoscale, traditional three-dimensional (3D) FE materials may become incompetent, since their ferroelectric properties are usually severely suppressed due to the depolarization field and surface reconstruction with dangling bonds [2]. The rise of low-dimensional materials opens up a new platform for searching ferroelectrics for next generation micro-electro-mechanical systems [13–17]. Compared with traditional 3D counterparts, low-dimensional materials are easier to be manipulated, naturally suitable for the miniaturized devices. The study of two-dimensional polar systems started from the graphene monolayer functionalized by hydroxyl groups [18, 19].

Later, intrinsic ferroelectricity has also been achieved or predicted in many monolayers or few-layers, most of which are exfoliated from van der Waals (vdW) materials [20–27].

The dimension of FE materials can be further reduced to one-dimensional (1D). For example, organic PVDF-TrFE nanowire [28], group-IV metal chalcogenides nanowires [29], and BiN/SbN nanowires [30] were confirmed/predicted to exhibit ferroelectricity. In addition, quasi-1D ferroelectricity was also predicted in vdW oxyhalides WOX_4 ($X=\text{Cl}, \text{Br}, \text{and I}$) [31]. The 1D antiferroelectric (AFE) materials are also predicted, such as CsTaS_3 [32]. Even though, the known 1D FE/AFE materials remain rare, and more seriously the experimental realization of these 1D polar materials remains challenging. Therefore, it is urgent to explore more suitable (quasi)-1D FE/AFE materials, especially those can be easily synthesized and manipulated.

NbOX_3 ($X=\text{Cl}, \text{Br}, \text{and I}$) bulks with vdW interactions between 1D double-chains were experimentally synthesized many years ago [33–35], which were found to own polar structures. Recently, Zhang *et al.* investigated the FE properties of the individual double-chain of NbOX_3 [36], confirming their ferroelectricity in the 1D limit. Thus, as an experimentally-existing series, this Nb-based oxyhalide family is highly important as a prototype model system to explore the 1D ferroelectricity. However, there are still many unresolved physical issues for NbOX_3 , especially for their bulk structures. The geometry of vdW double-chains allows different configurations of FE dipoles, leading to different polar phases. In Ref. [36], the intra-chain AFE and FE configurations were considered, whereas the inter-chain configurations (including the chain stacking and dipole alignments) were not touched.

In this paper, we thoroughly investigate the stability and polarity of NbOX_3 bulk structures using first-principles calculations. The different stacking patterns of

* Email: wangss@seu.edu.cn

† Email: sdong@seu.edu.cn

these 1D double-chains lead to the presence of seven possible polar phases within the tetragonal and monoclinic frameworks. Our calculation confirms that the displacements of Nb ions break the local inversion symmetry, which lead to robust ferroelectricity or antiferroelectricity in bulks. The proximate energies of FE and AFE phases allow possible MPB's in these systems, whereas the original experimental x-ray diffraction (XRD) patterns might miss the FE phase. Furthermore, a moderate hydrostatic pressure can tune the phase transitions between the tetragonal and the monoclinic structures.

II. COMPUTATIONAL METHODS

Our first-principles density functional theory (DFT) calculations are carried out using the Vienna *ab initio* simulation package in the framework of density functional theory [37]. The projector augmented wave method is adopted to deal with the interaction between electrons and ions [38]. The exchange-correlation functional is modeled by the generalized gradient approximation parameterized by Perdew, Burke, and Ernzerhof (PBE) [39]. Although Nb is a transition metal ion, its $4d$ orbitals are empty in the Nb^{5+} state. Thus, the Hubbard U repulsion has little influence on the physical properties of NbOX_3 . Therefore, our calculations are based on the pure PBE method, as performed for WOX_4 [31].

The energy cutoff for the plane-wave basis is set to be 520 eV. The Monkhorst-Pack k -mesh of $3 \times 3 \times 9$ is adopted for the Brillouin zone (BZ) sampling for both the tetragonal and monoclinic lattices. The lattice constants and ionic positions are fully optimized until the residual force on each atom is less than 0.005 eV/Å. The energy convergence criterion is set to be 10^{-6} eV. Besides, to accurately describe the vdW interaction between double-chains, zero damping DFT-D3 of Grimme correction is applied [40].

Dynamical stability is demonstrated by phonon spectral calculations based on finite differences and PHONOPY [41]. The phonon modes are analyzed by the AMPLIMODES software [42]. The ferroelectric polarization is calculated using the Berry phase method [43, 44]. The piezoelectric coefficient is calculated based on via finite differences [45].

In recent years, machine learning interatomic potentials becomes more and more popular to predict material structures and properties [46–48], which can be more efficient than conventional DFT, especially for those large systems. However, the systems involved here are unit cells (u.c.s) with only 20 ions. Then the DFT calculation is more suitable to deal with the subtle balance of candidate phases.

Besides the ground state, the thermal stability has also been checked using the *ab-initio* molecular dynamics (AIMD) simulations.

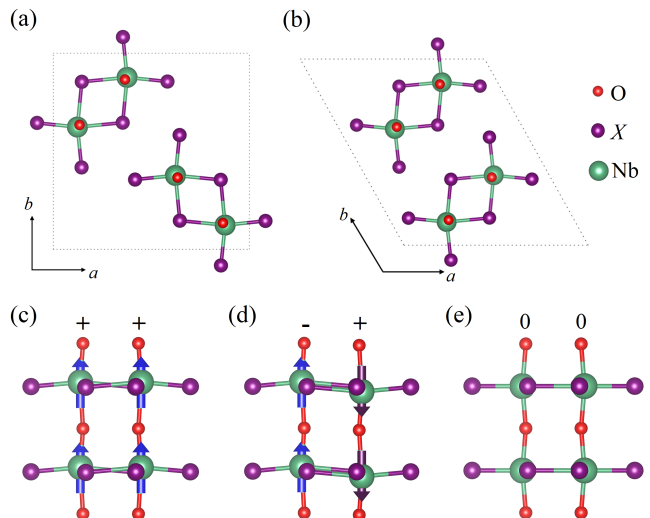


FIG. 1. Crystal structures of the NbOX_3 family. (a) and (b) are the top views of tetragonal and monoclinic lattices, respectively. (c)-(e) are 1D double-chains of FE, AFE, and paraelectric (PE) states, respectively. The symbols $+/-$ indicate the directions of polarizations. The blue/purple arrows represent $+/-$ polar direction along the c axis.

III. RESULT AND DISCUSSION

A. Structures of bulk NbOX_3

Such as WOX_4 and VOI_2 [31, 49], NbOX_3 series belong to the family of transition metal oxyhalides, which can be synthesized in experiments from reactions of niobium oxide and halogen at high temperatures [33–35]. The experimental structures of NbOX_3 family are shown in Figs. 1(a) and 1(b). In particular, NbOCl_3 and NbOBr_3 own the tetragonal phase, whereas NbOI_3 owns the monoclinic one, both of which consist of a pair of 1D double-chains in each u.c. The double-chains are coupled via vdW interaction, forming quasi-1D structures. Within each chain, each niobium is within an octahedral cage, which is formed by four planar halogen ions and two apical oxygen ions. Then two parallel NbO_2X_4 chains are linked into a dimer via a shared edge of two halogen ions, forming a unique double-chain. In contrast, the vdW structure in WOX_4 is consisted of single chains.

Since the nominal value of Nb is +5 here, its $4d^0$ electron configuration will be a primary driving force for polar instability. According to the experimental structure, all Nb ions exhibit relative displacements from the center of octahedra along the Nb-O-Nb 1D chain direction, leading to local dipoles. In the previous study, two polar structures of 1D NbOX_3 double-chain have been explored [36]. The FE and AFE structures are shown in Figs. 1(c) and 1(d), where the dipoles in two parallel chains are parallel and antiparallel, respectively. For reference, the centrosymmetric PE phase is shown in Fig. 1(e), without the displacements of Nb ions along the chain direction.

Their calculations found the 1D FE phase is energetically more stable than the AFE one (0.1/1.0/1.1 meV/Nb for Cl/Br/I) [36].

In the following, we will explore the polarity of NbOX_3 beyond the simple 1D double-chain, but focus on the more realistic bulks. Since its unit cell contains a pair of 1D double-chains, there are more possible configurations, including: (1) the bulk FE states with all Nb dipoles pointing to the same directions ($++$, $++$); (2) the bulk AFE phases (named as AFE-1) consisted of 1D FE double-chains with opposite dipoles ($++$, $--$); (3) the AFE-2 ($+-$, $-+$) and AFE-3 ($+-$, $+-$) structures consisted of 1D AFE double-chains with different stacking modes, as shown in Fig. S1 in the Supplemental Materials (SM) [50]. For the tetragonal crystals, the AFE-2 and AFE-3 structures are identical due to symmetry.

Our calculated results are summarized in Table I. It is clear that all DFT optimized lattice constants are close to the corresponding experimental values. For NbOI_3 , the ground state is indeed in the monoclinic FE phase, whereas the tetragonal phases are definitely higher in energy. In contrast, the tetragonal structures of NbOCl_3 and NbOBr_3 are more stable than their monoclinic counterparts. Both these results agree with experimental structures [34, 35].

Surprisingly, it is noted that the calculated ground states of both NbOCl_3 and NbOBr_3 are tetragonally FE (teFE) phases, which are slightly lower in energy (~ 1 meV/u.c.) than the tetragonal AFE-1 (teAFE-1) expected from the experimental structure [34, 35]. Such tiny energy differences between the teFE and the teAFE-1 phases are reasonable considering the weak interchain vdW interaction. Since the DFT calculation is for the zero-temperature ground state. Then the experimental teAFE-1 phase may exist at an ambient condition due to the thermal excitation or entropy effect. In fact, such proximate energies and structures may allow the phase coexistence (and MPB) in real materials.

To verify this hypothesis, we simulated the powder XRD patterns of tetragonal NbOCl_3 using vesta [51], based on our optimized structures. As shown in Fig. S2 in the SM [50], there are indeed some characteristic peaks e.g. (201) and (401), to distinguish the PE and AFE-1 phases, as used in the early XRD experiment to identify the AFE-1 phase [34]. However, the XRD patterns are extremely similar between the FE and the AFE-1 phases, without any distinct peak in the measuring region. It was possible the reason why the early XRD measurement did not identify the teFE phases.

B. Dynamic stability and evolution under pressure

Taking the tetragonal NbOCl_3 and monoclinic NbOI_3 as examples, the phonon spectra and symmetry analyses are performed to investigate the dynamic stability and the evolution of phases.

As shown in Fig. 2(a), there are four branches of

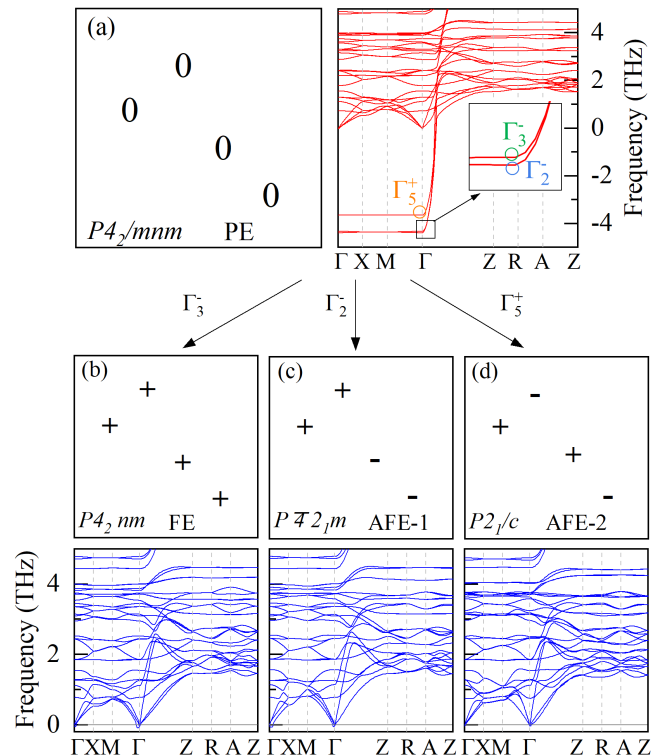


FIG. 2. Distortion modes and phonon spectra of tetragonal NbOCl_3 . (a) PE; (b) FE; (c) AFE-1; (d) AFE-2. The inset of (a): the magnified view to distinguish the almost degenerate Γ_3^- and Γ_2^- .

imaginary frequencies crossing the center and edge of the BZ for the phonon spectrum of tetragonal PE NbOCl_3 . Specifically, the Γ_3^- mode leads to the FE phase [Fig. 2(b)], and the Γ_2^- mode leads to the AFE-1 phase [Fig. 2(c)]. As aforementioned, the difference between the FE and the AFE-1 is only the inter-chain coupling: parallel vs anti-parallel, whereas their intra-chain distortions are identical. Thus, these Γ_3^- and Γ_2^- modes are almost degenerate in imaginary frequencies. Another double-degenerate Γ_5^+ mode leads to AFE-2 (or equivalent AFE-3) bulk structure [Fig. 2(d)]. There is no any imaginary frequency in the phonon spectra of FE, AFE-1, and AFE-2 phases, indicating their dynamic stabilities.

Similar analyses are also performed for monoclinic NbOI_3 . As shown in Fig. 3(a), there are also four imaginary frequencies located at the center of the BZ in the phonon spectrum of the PE phase. The higher two modes (Γ_1^- and Y_1^-) are almost degenerate, which lead to the FE and AFE-1 phases, respectively. The lower two modes (Y_2^+ and Γ_2^+) are almost degenerate too, which lead to the AFE-2 and AFE-3 phases, respectively. Also, for all these four FE/AFE phases, they are dynamically stable since no imaginary frequency exist in their phonon spectra, as shown in Figs. 3(b) and 3(e).

More phonon spectra of monoclinic NbOCl_3 , tetragonal NbOI_3 , and monoclinic/tetragonal NbOBr_3 can be found in the SM (Figs. S3-S6) [50]. Their physical sce-

TABLE I. DFT results of the NbOX_3 family, in comparison with the experimental (EXP) results. The lattice constants (a , b , and c) are in units of angstroms. The volume of unit cell (V) is in units of \AA^3 . The energy differences ΔE are in units of meV/u.c., and the energy of monoclinic FE phase is taken as a reference. The lowest energy ones are emphasized in bold. The band gap is in units of eV.

Material	Crystal	Phase	Space group	a	b	c	ΔE	V	Gap
NbOCl_3	Monoclinic	PE	$I2/m$	11.020	12.705	3.817	136.68	466.88	1.35
		FE	$I2$	10.953	12.645	3.920	0	473.47	2.75
		AFE-1	$P2/b$	10.928	12.637	3.921	1.32	472.78	2.77
		AFE-2	$P2_1/b$	10.927	12.632	3.921	1.91	472.78	2.77
		AFE-3	$C\bar{1}$	10.933	12.630	3.922	1.06	473.03	2.75
	Tetragonal	PE	$P4_2/mnm$	11.048		3.817	126.50	465.81	2.44
		FE	$P4_2/nm$	10.982		3.918	-6.10	473.26	2.83
		AFE-1	$P4_2m$	10.988		3.919	-4.86	472.67	2.83
		AFE-2	$P2_1/C$	10.982		3.919	-4.11	472.52	2.84
		EXP	$P4_2m$	10.896		3.948			
NbOBr_3	Monoclinic	PE	$I2/m$	11.744	13.553	3.832	92.49	529.81	1.78
		FE	$I2$	11.703	13.531	3.914	0	536.99	1.95
		AFE-1	$P2/b$	11.673	13.511	3.911	1.34	535.85	1.99
		AFE-2	$P2_1/b$	11.660	13.510	3.909	4.29	535.84	1.93
		AFE-3	$C\bar{1}$	11.662	13.502	3.910	5.3	534.64	1.93
	Tetragonal	PE	$P4_2/mnm$	11.756		3.817	88.15	529.30	1.71
		FE	$P4_2/nm$	11.699		3.910	-1.63	535.18	1.93
		AFE-1	$P4_2m$	11.606		3.905	-0.53	535.25	1.91
		AFE-2	$P2_1/C$	11.707		3.908	3.24	535.19	1.91
		EXP	$P4_2m$	11.636		3.953			
NbOI_3	Monoclinic	PE	$I2/m$	12.778	14.795	3.878	46.32	633.53	0.61
		FE	$I2$	12.738	14.764	3.939	0	640.00	0.76
		AFE-1	$P2/b$	12.744	14.759	3.938	3.14	638.73	0.76
		AFE-2	$P2_1/b$	12.730	14.762	3.937	6.12	639.60	0.74
		AFE-3	$C\bar{1}$	12.726	14.756	3.936	6.55	638.85	0.78
	Tetragonal	EXP	$I2$	12.602	14.624	3.991			
		PE	$P4_2/mnm$	12.768		3.876	59.53	631.88	0.52
		FE	$P4_2/nm$	12.723		3.937	16.45	637.22	0.70
		AFE-1	$P4_2m$	12.709		3.936	19.05	635.70	0.67
		AFE-2	$P2_1/C$	12.729		3.934	21.76	637.24	0.65

narios are quite similar.

According to above analyses, there are seven possible stable structures for each NbOX_3 crystal. It can be seen from Table I that their energies are rather proximate, especially for NbOCl_3 and NbOBr_3 . These small energy differences (on the order of 1 meV/Nb) make it highly possible to tune these phases using external stimulations. For example, a hydrostatic pressure may drive the monoclinic ones to tetragonal phases, since the tetragonal ones always own smaller volumes, as compared in Table I. Since the ground states of NbOCl_3 and NbOBr_3 are already the tetragonal phases, this pressure driven phase transition can only occur in NbOI_3 whose ground state is monoclinic.

To investigate possible structural phase transition, the structures of NbOI_3 are optimized under hydrostatic pressures. The enthalpies are compared to determined the possible ground states under the pressure, as shown in Fig. 4(a). It is clear that NbOI_3 will turn to be tetragonal when pressure is larger than 2 GPa. The evolution of lattice constants are shown in Fig. 4(b). Under expectation, the in-plane lattice constants shrink much larger than the out-of-plane one, due to the anisotropic stiffness.

The vdW interaction between chains make the material softer on the ab plane. For the monoclinic phase, the b axis is even more softer than the a axis, in agreement with the intuitive view of its structure [Fig. 1(b)]. Meanwhile, the lattice angle between the a - b axes of the monoclinic phase also decreases with pressure, also shown in Fig. 4(b).

C. Ferroelectricity and piezoelectricity

The polarization is a key physical quantity of a FE material. Here the spontaneous polarizations of $\text{NbOCl}_3/\text{NbOBr}_3/\text{NbOI}_3$ are estimated to be 24.3/19.8/14.2 $\mu\text{C}/\text{cm}^2$ for tetragonal FE phases, and 27.2/20.0/15.27 $\mu\text{C}/\text{cm}^2$ for monoclinic FE phases, respectively, as shown in Fig. 5(a). Due to the quasi-1D characteristic, these values are almost identical for those meta-stable structures, i.e., monoclinic $\text{NbOCl}_3/\text{NbOBr}_3$ and tetragonal NbOI_3 , as well as the single double-chains [36]. The decreasing polarization from $X=\text{Cl}$ to I is mainly due to the increasing volume. Luckily, all these polarizations are moderate, comparable to that of

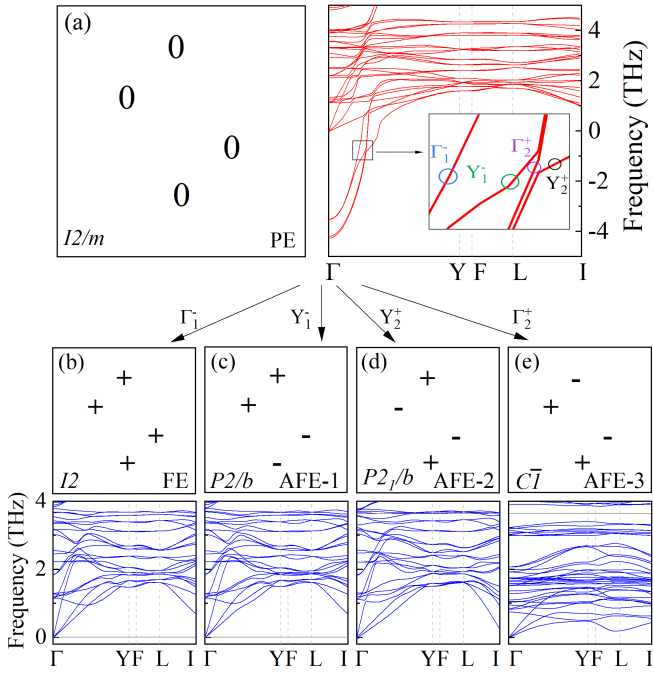


FIG. 3. Distortion modes and phonon spectra of monoclinic NbOI_3 . (a) PE; (b) FE; (c) AFE-1; (d) AFE-2; (e) AFE-3. The inset of (a): the magnified view to distinguish the almost degenerate Γ_1^- and Y_1^- , as well as Γ_2^+ and Y_2^+ .

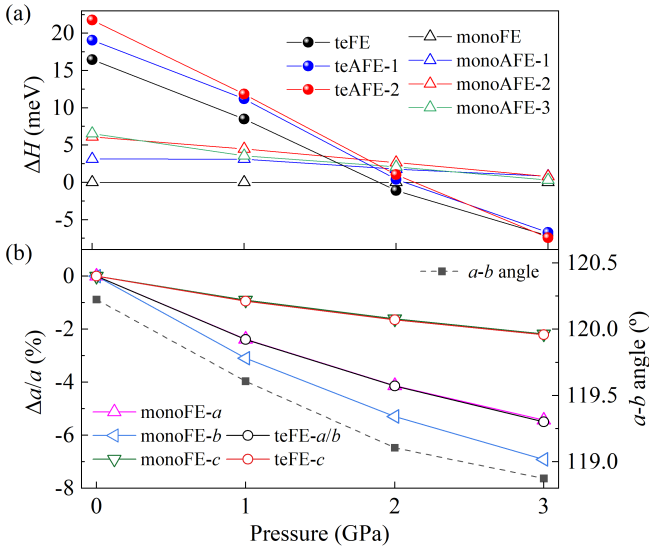


FIG. 4. (a) The relative enthalpies (per u.c.) of various phases of NbOI_3 as a function hydrostatic pressure. The monoclinic FE phase is taken as the reference. (b) The relative changes of lattice constants (left) and lattice angle between the a - b axes (right) under pressure. Only the FE phase is illustrated as an example, whereas the tendencies of other AFE phases are similar.

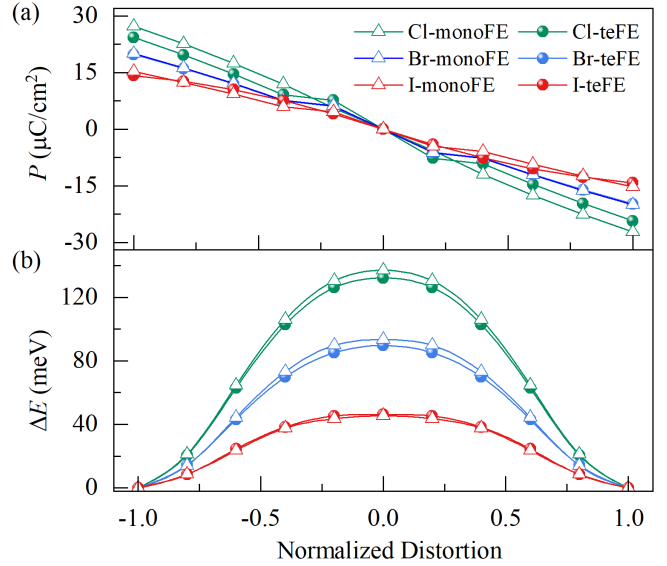


FIG. 5. Ferroelectric switching of NbOX_3 bulks. (a) Polarization and (b) energy barriers (per u.c.) as a function of the FE distortion intensity. Two end states (± 1) denote the optimized FE states ($\pm P$), and the middle one is the optimized PE states. Other intermiddle points are obtained using structural interpolation.

the commercially used perovskite BaTiO_3 ($\sim 20 - 25 \mu\text{C}/\text{cm}^2$).

Besides the polarization, the coercive field is also an essential property of a FE system, which is, in principle, related to the energy cost of FE switching barrier. Seven possible flip paths are considered, in which the transition states include PE, FE, AFE-1, AFE-2 and AFE-3 phases (for monoclinic structures only), as shown in Fig. S7 of the SM [50]. The calculation results show that the FE-PE flip path has the lowest potential barrier for all three cases. As shown in Fig. 5(b), the estimated barrier of $\text{NbOCl}_3/\text{NbOBr}_3/\text{NbOI}_3$ is 132/89/46 meV/u.c. (i.e., 33/22/12 meV/f.u.) for tetragonal FE phases, and 137/93/45 meV/u.c. (i.e., 34/23/11 meV/f.u.) for monoclinic NbOI_3 , which is comparable to that of BaTiO_3 (~ 34 meV/f.u.) [31]. Noting here these barriers can only be considered as theoretical upper limits, whereas other switching paths may exist which can further reduce the barriers.

The ferroelectricity of NbOX_3 can be described by a classical polarization model based on the Landau-Ginzburg-Devonshire formula [52]:

$$E = \frac{\alpha}{2}P_1^2 + \frac{\beta}{4}P_1^4 + \frac{\gamma}{6}P_1^6 + \frac{\alpha}{2}P_2^2 + \frac{\beta}{4}P_2^4 + \frac{\gamma}{6}P_2^6 + \frac{\delta}{2}(P_1^2 - P_2^2)^2, \quad (1)$$

where P_1 and P_2 denote the (local) polarization from double-chains 1 and 2, respectively, and the last item corresponds to the interchain coupling. All these coefficients can be obtained by fitting the polarization-potential curves. The coefficients of the NbOX_3 FE phases and the fitting polarization-energy barrier curves

are shown as Table S1 and Fig. S8 of the SM [50]. The calculation results show that the values of δ are substantially smaller than that of α , indicating the inter-chain coupling is weak.

Besides ferroelectricity, piezoelectricity is another important physical property for FE materials. Crystallographic symmetry analysis shows that the elastic matrix C 's have 7 and 13 independent non-zero coefficients for the tetragonal and monoclinic lattices respectively [53]. The piezoelectric stress tensor matrix e of tetragonal (monoclinic) crystal has four- (five-) independent matrix elements [54]. Then the piezoelectric strain coefficient calculation formula can be expressed as:

$$d_{ij} = \sum_{k=1}^6 e_{ik} S_{kj}, \quad (2)$$

where S denotes the tensor of the elastic compliance coefficient ($S = C^{-1}$). The key piezoelectric coefficient d_{33} represents the piezoelectric constant when the polarization direction is the same as the stress direction. Here the calculated piezoelectric d_{33} 's are 34.6/36.9/60.1 pC/N for FE tetragonal NbOCl₃/NbOBr₃ and monoclinic NbOI₃ phases, respectively. All these d_{33} 's are larger than those of quasi-1D WOX₄ (where their d_{33} =27.3/27.7/39.8 pC/N for $X = \text{F/Cl/Br}$) [31], as well as the conventional piezoelectric ZnO (d_{33} = 12.3 pC/N) [55]. Note that the theoretical d_{33} 's should be considered to be lower limits, whereas in real materials the experimental d_{33} 's can be enhanced significantly by many other factors such as MPB and domain textures. More details of the elastic tensor C , the piezoelectric tensor e , and the piezoelectric strain tensors d are summarized in Table S2 of the SM [50].

The thermal stability has also been checked. With a $1 \times 1 \times 5$ supercell, our AIMD simulations at 500 K for 5 ps show robust structures for both the tetragonal NbOX₃ ($X=\text{Cl/Br}$) and monoclinic NbOI₃, as shown in Fig. S9 of SM [50].

Furthermore, the SOC has also been tested on the NbOI₃ ground state, which owns the heaviest atom iodine. However, the lattice constants, band gap, and polarization are almost unchanged with SOC, as shown in Table S3 of the SM [50]. Physically, the impact of SOC on NbOCl₃ and NbOBr₃ should be even weaker. Such negligible SOC effects are reasonable, since all of them are band insulators with fully occupied/empty bands.

IV. CONCLUSION

To summarize, the quasi-1D NbOX₃ bulks have been systematically studied, going beyond the individual double-chain scenario but considering more realistic fact of inter-chain interactions. From the parent PE phases, seven possible FE or AFE states are derived according to the symmetry analyses, whose dynamic stabilities are further confirmed by phonon spectra. The FE and AFE phases are energetically proximate, which may allow the coexisting in real materials at ambient conditions. And for NbOI₃ the monoclinic to tetragonal structural transition can be triggered by a small hydrostatic pressure. The polarities of FE NbOX₃ are prominent, with considerable spontaneous polarizations, moderate switching barriers, and large piezoelectric d_{33} coefficients, which allow promising potentials for applications.

ACKNOWLEDGMENTS

This work was supported by National Natural Science Foundation of China (Grants No. 11834002 and No. 12104089), Natural Science Foundation of Jiangsu Province (Grant No. BK20200345) the Fundamental Research Funds 357 for the Central Universities. We acknowledge the computational source from the Big Data Center of Southeast University.

-
- [1] K. M. Rabe, M. Dawber, C. Lichtensteiger, C. H. Ahn, and J.-M. Triscone, *Physics of Ferroelectrics* (Springer, Berlin, 2007).
 - [2] M. Dawber, K. M. Rabe, and J. F. Scott, *Rev. Mod. Phys.* **77**, 1083 (2005).
 - [3] F. Xue, J.-H. He, and X. Zhang, *Appl. Phys. Rev.* **8**, 021316 (2021).
 - [4] S. Zhou, L. You, H. Zhou, Y. Pu, Z. Gui, and J. Wang, *Front. Phys.* **16**, 13301 (2021).
 - [5] Z. L. Wang, *Mater. Today* **10**, 20 (2007).
 - [6] J. Briscoe and S. Dunn, *Piezoelectricity and ferroelectricity* (Springer, Berlin, 2014).
 - [7] B. Noheda, J. A. Gonzalo, L. E. Cross, R. Guo, S.-E. Park, D. E. Cox, and G. Shirane, *Phys. Rev. B* **61**, 8687 (2000).
 - [8] Z.-G. Ye, *Handbook of advanced dielectric, piezoelectric and ferroelectric materials: Synthesis, properties and applications* (Elsevier, Amsterdam, 2008).
 - [9] R. Guo, L. E. Cross, S. E. Park, B. Noheda, D. E. Cox, and G. Shirane, *Phys. Rev. Lett* **84**, 5423 (2000).
 - [10] Z. Wu and R. E. Cohen, *Phys. Rev. Lett* **95**, 037601 (2005).
 - [11] H. Fu and R. E. Cohen, *Nature* **403**, 281 (2000).
 - [12] S. Song, Y. Zhang, J. Guan, and S. Dong, *Phys. Rev. B* **103**, L140104 (2021).
 - [13] M. An and S. Dong, *APL Mater.* **8**, 110704 (2020).
 - [14] M. Wu, *ACS Nano* **15**, 9229 (2021).
 - [15] Z. Guan, H. Hu, X. Shen, P. Xiang, N. Zhong, J. Chu, and C. Duan, *Adv. Electron. Mater.* **6**, 1900818 (2020).
 - [16] H. P. You, N. Ding, J. Chen, and S. Dong, *Phys. Chem. Chem. Phys.* **22**, 24109 (2020).
 - [17] Z. Wang, N. Ding, C. Gui, S. S. Wang, M. An, and S. Dong, *Phys. Rev. Mater.* **5**, 074408 (2021).
 - [18] M. Wu, J. D. Burton, E. Y. Tsympal, X. C. Zeng, and P. Jena, *Phys. Rev. B* **87**, 081406(R) (2013).

- [19] E. Kan, F. Wu, K. Deng, and W. Tang, *Appl. Phys. Lett.* **103**, 193103 (2013).
- [20] W. Ding, J. Zhu, Z. Wang, Y. Gao, D. Xiao, Y. Gu, Z. Zhang, and W. Zhu, *Nat. Commun.* **8**, 14956 (2017).
- [21] C. Liu, W. Wan, J. Ma, W. Guo, and Y. Yao, *Nanoscale* **10**, 7984 (2018).
- [22] E. Bruyer, D. Di Sante, P. Barone, A. Stroppa, M.-H. Whangbo, and S. Picozzi, *Phys. Rev. B* **94**, 195402 (2016).
- [23] R. Fei, W. Kang, and L. Yang, *Phys. Rev. Lett.* **117**, 097601 (2016).
- [24] S. Guan, C. Liu, Y. Lu, Y. Yao, and S. A. Yang, *Phys. Rev. B* **97**, 144104 (2018).
- [25] M. Wu and X. C. Zeng, *Nano Lett.* **16**, 3236 (2016).
- [26] C. Xiao, F. Wang, S. A. Yang, Y. Lu, Y. Feng, and S. Zhang, *Adv. Funct. Mater.* **28**, 1707383 (2018).
- [27] N. Ding, J. Chen, C. Gui, H. You, X. Yao, and S. Dong, *Phys. Rev. Mater.* **5**, 084405 (2021).
- [28] Z. Hu, M. Tian, B. Nysten, and A. M. Jonas, *Nat. Mater.* **8**, 62 (2009).
- [29] J.-J. Zhang, J. Chen, S. Dong, and B. I. Yakobson, *J. Am. Chem. Soc.* **141**, 15040 (2019).
- [30] C. Yang, M. Chen, S. Li, X. Zhang, C. Hua, H. Bai, S. A. Yang, and Y. H. Lu, *ACS Appl. Mater. Interfaces* **13**, 13517 (2021).
- [31] L.-F. Lin, Y. Zhang, A. Moreo, E. Dagotto, and S. Dong, *Phys. Rev. Mater.* **3**, 111401(R) (2019).
- [32] J. Bie, J. Zhou, and W. Fa, *Adv. Theory Simul.* **5**, 2200022 (2022).
- [33] D. E. Sands, A. Zalkin, and R. E. Elson, *Acta Cryst.* **12**, 21 (1959).
- [34] M. Ströbele and H. J. Meyer, *Z. Anorg. Allg. Chem.* **628**, 488 (2002).
- [35] S. Hartwig and H. Hillebrecht, *Z. Anorg. Allg. Chem.* **634**, 115 (2008).
- [36] L. Zhang, C. Tang, S. Sanvito, and A. Du, *NPJ Comput. Mater.* **7**, 135 (2021).
- [37] G. Kresse and J. Furthmüller, *Phys. Rev. B* **54**, 11169 (1996).
- [38] P. E. Blöchl, *Phys. Rev. B* **50**, 17953 (1994).
- [39] J. P. Perdew, K. Burke, and M. Ernzerhof, *Phys. Rev. Lett.* **77**, 3865 (1996).
- [40] S. Grimme, J. Antony, S. Ehrlich, and H. Krieg, *J. Chem. Phys.* **132**, 154104 (2010).
- [41] A. Togo and I. Tanaka, *Scripta Mater.* **108**, 1 (2015).
- [42] D. Orobengoa, C. Capillas, M. I. Aroyo, and J. M. Perez-Mato, *J. Appl. Crystallogr.* **42**, 820 (2009).
- [43] R. Resta, *Rev. Mod. Phys.* **66**, 899 (1994).
- [44] R. D. King-Smith and D. Vanderbilt, *Phys. Rev. B* **47**, 1651 (1993).
- [45] Y. Le Page and P. Saxe, *Phys. Rev. B* **65**, 104104 (2002).
- [46] I. S. Novikov, K. Gubaev, E. V. Podryabinkin, and A. V. Shapeev, *Mach. Learn.: Sci. Technol.* **2**, 025002 (2021).
- [47] B. Mortazavi, B. Javvaji, F. Shojaei, T. Rabczuk, A. V. Shapeev, and X. Zhuang, *Nano Energy* **82**, 105716 (2021).
- [48] B. Mortazavi, M. Silani, E. V. Podryabinkin, T. Rabczuk, X. Zhuang, and A. V. Shapeev, *Adv. Mater.* **33**, 2102807 (2021).
- [49] N. Ding, J. Chen, S. Dong, and A. Stroppa, *Phys. Rev. B* **102**, 165129 (2020).
- [50] See Supplemental Materials for more details of various polar/PE structures, phonon spectra, simulated powder XRD, multiple switching paths, the coefficients of Landau-Ginzburg-Devonshire formula and fitting polarization-energy barrier curves, elastic and piezoelectric coefficients, *ab-initio* molecular dynamics simulations and effects of spin-orbit coupling (SOC).
- [51] K. Momma and F. Izumi, *J. Appl. Cryst.* **44**, 1272 (2011).
- [52] L.-F. Lin, Y. Zhang, A. Moreo, E. Dagotto, and S. Dong, *Phys. Rev. Lett.* **123**, 067601 (2019).
- [53] F. Mouhat and F. X. Coudert, *Phys. Rev. B* **90**, 224104 (2014).
- [54] M. De Jong, W. Chen, H. Geerlings, M. Asta, and K. A. Persson, *Sci. Data* **2**, 150053 (2015).
- [55] X. Wu, D. Vanderbilt, and D. R. Hamann, *Phys. Rev. B* **72**, 035105 (2005).